ACS MATERIALS LETTERS

www.acsmaterialsletters.org

Enhanced Ion Conduction via a Diverse Cl-PS_4 Anion Lattice in Li_3PS_4–xLiCl

Pengbo Wang, Sawankumar Patel, Jason E. Roberts, Brian E. Francisco,* and Yan-Yan Hu*

Cite This: *ACS Materials Lett.* 2024, 6, 2059–2064

Read Online

ACCESS | Metrics & More | Article Recommendations | Supporting Information

ABSTRACT: **Thiophosphates show promise as solid electrolytes for all-solid-state batteries (ASSBs), particularly Li_3PS_4-based materials, due to their cost-effectiveness and stability. To enhance conductivity for high-power applications, we developed affordable Li_3PS_4-LiCl (LPSCls) solid electrolytes with an ionic conductivity of ∼1.1 mS/cm (Li_3PS_4:LiCl = 2:1, 200 °C). Our study examines the long- and short-range structural order and ion dynamics of LPSCls, using neutron diffraction, magic-angle-spinning nuclear magnetic resonance (MAS NMR), and electrochemical impedance spectroscopy (EIS). ^{31}P NMR reveals a unique disordered anion structure comprising a blend of Cl-modified β, γ, and amorphous PS_4^{3-} units. Additionally, NMR relaxometry highlights enhanced Li^+ mobility enabled by this diverse anion sublattice, allowing Li^+ ions to migrate efficiently among different anions with similar affinity. Our findings unveil novel anion species within LPSCls, offering insights for optimizing ionic conductivity in solid electrolytes for ASSBs.**

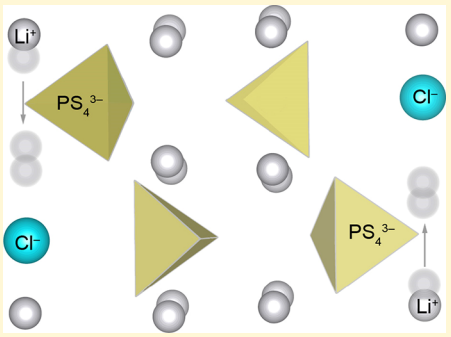

Mass adoption of electric vehicles requires exploring cutting-edge energy storage solutions beyond the conventional Li-ion batteries to alleviate the range anxiety caused by limited energy density. Solid-state batteries (SSBs) have emerged as one of the most promising technologies in this pursuit,[1] offering improved energy density through the utilization of lithium metal anodes[2] and a bipolar stacking[3,4] structure. Moreover, SSBs hold the potential for significantly improving safety by replacing the combustible carbonate-based electrolytes with more thermally stable ceramic/glass materials.[5]

High-performance SSBs rely on state-of-the-art solid electrolytes to enable rapid ion conduction. Recent research on Li-argyrodites has showcased how fine-tuning the anion substructures can lead to enhanced Li^+-ion conduction,[6−9] opening a promising avenue for improving Li^+ ion conductivity in other materials. Among the thiophosphates, Li_3PS_4 has garnered substantial attention, leading to the development of various novel solid electrolytes, such as crystalline $Li_{10}P_3S_{12}I$,[10] $Li_7P_2S_8I$,[11] $Li_7P_2S_8X$ (X = I, Br),[12] $Li_{15}P_4S_{16}Cl_3$,[13] Li_3PS_4-LiBr,[14] and Li_3PS_4-LiI.[15] However, the structural complexity of Li_3PS_4 and its derivatives presents a challenge in understanding the correlation between their anion substructure and Li^+ ion conduction. Therefore, systematic investigations with an approach that permits multiscale structural visualization become imperative.

The complexity of Li_3PS_4 stems from its distinctive polymorphs and diverse short-range structures. Li_3PS_4 has four different structures: a low-temperature γ-phase, an intermediate-temperature β-phase, a high-temperature α-phase, and a high-pressure δ-phase.[16,17] Previous studies have revealed that the Li^+-ion conductivity of Li_3PS_4 is influenced not only by its long-range structures but also by the short-range structures, which often exhibit a strong correlation to the synthesis protocols. For example, β-Li_3PS_4 and γ-Li_3PS_4 synthesized through a solid-state approach exhibit conductivities of 9×10^{-7} S/cm and 2.6×10^{-7} S/cm, respectively, while a nanoporous β-Li_3PS_4 synthesized via a solvent-mediated method shows a significantly higher conductivity of 1.6×10^{-4} S/cm.[18] However, a later systematic study on this nanoporous β-Li_3PS_4 has revealed that the so-called "nanoporous β-Li_3PS_4" is, in fact, a mixture of crystalline β-Li_3PS_4, amorphous Li_3PS_4, and solvent-containing Li_3PS_4·2THF.[19] The amorphous phase is more conductive than its crystalline counterpart.[19] Moreover, the conductivity decreases with the increasing the content of β-Li_3PS_4.[19,20] Thus, understanding the highly disordered structural components holds great significance for developing Li_3PS_4-derived materials, as it will provide valuable insights into the precise tuning of the crystalline/amorphous/solvent-modified Li_3PS_4 phases to achieve optimal conductivity.

Received: March 7, 2024
Revised: April 9, 2024
Accepted: April 16, 2024
Published: April 18, 2024

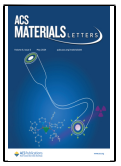

https://doi.org/10.1021/acsmaterialslett.4c00488
ACS Materials Lett. 2024, 6, 2059–2064

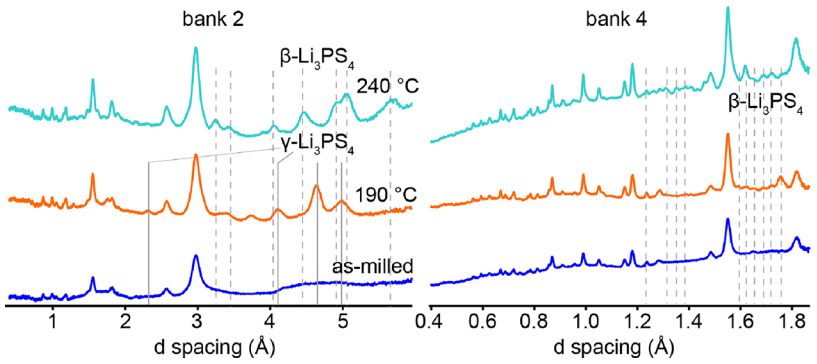

Figure 1. Neutron Bragg diffractions of LPSCls (Li_3PS_4:LiCl = 2:1) synthesized with different conditions: as-milled, 190 °C, and 240 °C. Diffractions from bank 4 (high *d*-spacing) and bank 2 (low *d*-spacing) are presented side by side.

Here, we developed novel Li_3PS_4−LiCl (LPSCls) composite electrolytes. Considering that the conductivity of Li_3PS_4-derived materials depends on the synthesis conditions, different synthesis temperatures and their effects on the structure were carefully investigated. We achieved the highest conductivity (∼1.1 mS/cm, Li_3PS_4:LiCl = 2:1), with a synthesis temperature of 200 °C. -MAS NMR and ^{7}Li spin−lattice NMR relaxometry results elucidate that the highest conductivity arises from the disordered anion substructures, which is manifested by the presence of multiple distinctive PS_4^{3-} units: γ-PS_4^{3-}··Cl^-, β-PS_4^{3-}··Cl^-, and amorphous-PS_4^{3-}··Cl^-. Understanding the diverse anion structure units paves the way for optimizing the ionic conductivity of thiophosphate materials.

Since the structures of Li_3PS_4 and its derivatives are highly dependent on the synthesis temperatures, differential scanning calorimetry (DSC) was measured within a range of 50−400 °C (Figure S1) to explore the possible phase transitions of LPSCl (Li_3PS_4:LiCl = 2:1). The results suggest that the as-milled LPSCl undergoes two distinctive phase transitions at 190 and 240 °C, respectively. A rapid exothermic heat release marks the phase transition at 190 °C, while the second transition spans a broader temperature range from 220 °C to 240 °C, suggesting a potential gradual shift in the long/short-range structural order. To investigate the change in the long-range structural order (Figure S1), neutron Bragg diffraction is employed for its capability to differentiate light elements such as Li, S, and Cl. As shown in Figure 1, LPSCls contain a great amount of amorphous phase, and the major difference among them lies in the diffractions from 4 Å to 6 Å. Upon the annealing at 190 °C, the crystalline phases γ-Li_3PS_4 and β-Li_3PS_4 emerge. It is noted that this 190 °C-sample adopts a unique hybrid structure that integrates the high *d*-spacing structural motif of γ-Li_3PS_4 (Figure 1, left) and the lower *d*-spacing structural pattern of β-Li_3PS_4 (Figure 1, right).

With the annealing at 240 °C, the LPSCl crystalizes into a lattice similar to β-Li_3PS_4. Since the Bragg diffraction indicates that a great fraction of LPSCl $_4$ exists in a low-crystallinity phase with only short-range ordering, accurate analysis solely based on the Bragg peaks is challenging. Investigations into the short-range structures using approaches that offer direct insights into shorter length scales are necessary. In the following sections, we present the neutron pair distribution functions and multi-nuclear NMR results to harness this capability and construct a comprehensive multiscale depiction of the LPSCl structure.

For solid electrolytes, ion conduction can be greatly impacted by short-range structures, especially for glass-ceramic materials. To investigate the local atomic correlations, neutron pair distribution functions (nPDF), $G(r)$ of LPSCls (Li_3PS_4:LiCl = 2:1) are generated based on the total scattering data. Figure 2 shows the correlations within 5 Å. The negative

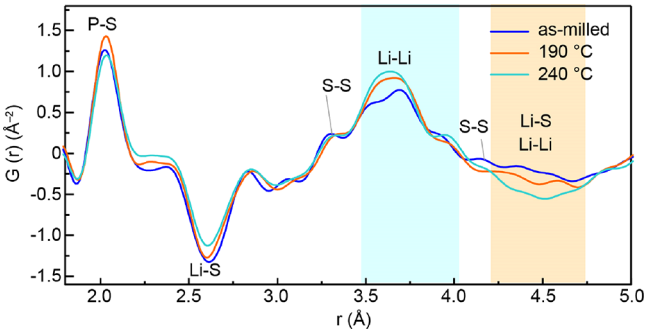

Figure 2. Short-range structural order of LPSCls (Li_3PS_4:LiCl = 2:1) (as-milled, 190 °C, and 240 °C) revealed by neutron pair distribution functions (nPDF).

peak ∼2.61 Å arises from the Li−S correlation in the Li_3PS_4.[21] Upon annealing, a decrease in the intensity and a shift toward a smaller real-space distance (r) are observed for Li−S. A short-range Li−Li correlation occurs at ∼3.6 Å.[21] Compared with the as-milled LPSCl, the annealed samples show larger intensities and a more smeared-out feature for the short-range Li−Li pairs. The long-range Li−Li correlation occurs within the region [4.2, 4.75], which overlaps with P−S and Li−S.

The inherent structural complexity LPSCls poses a significant challenge in distinguishing the highly disordered amorphous phase based on neutron diffractions. Therefore, MAS NMR is employed to examine the short-range structural order in LPSCls. The main ^{7}Li resonance of LPSCls shows a narrow and symmetric line shape (Figure 3a), indicating fast mobility and exchange of Li^+ ions. The annealing at a higher temperature moves the main peak toward a larger chemical shift. For comparison, the spectrum of LPS is presented above (Figure 3a). In contrast, the main peak of LPS (β-Li_3PS_4) is asymmetric, because of the distribution of Li at different crystallographic sites: Li1/Li2 at lower field and Li3 at higher field.[22] Furthermore, the original Li environments in the β and γ phase are absent in LPSCls, which indicates that the presence of Cl can modify the anion sublattice and enable Li^+ self-

https://doi.org/10.1021/acsmaterialslett.4c00488
ACS Materials Lett. 2024, 6, 2059−2064

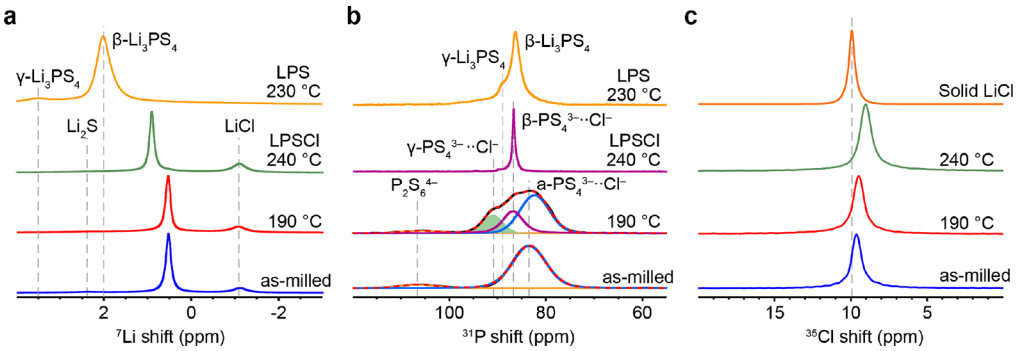

Figure 3. Short-range structural order of LPSCls (Li_3PS_4:LiCl = 2:1) (as-milled, 190 °C, and 240 °C) revealed by (a) ^{7}Li NMR, (b) ^{31}P NMR, and (c) ^{35}Cl NMR.

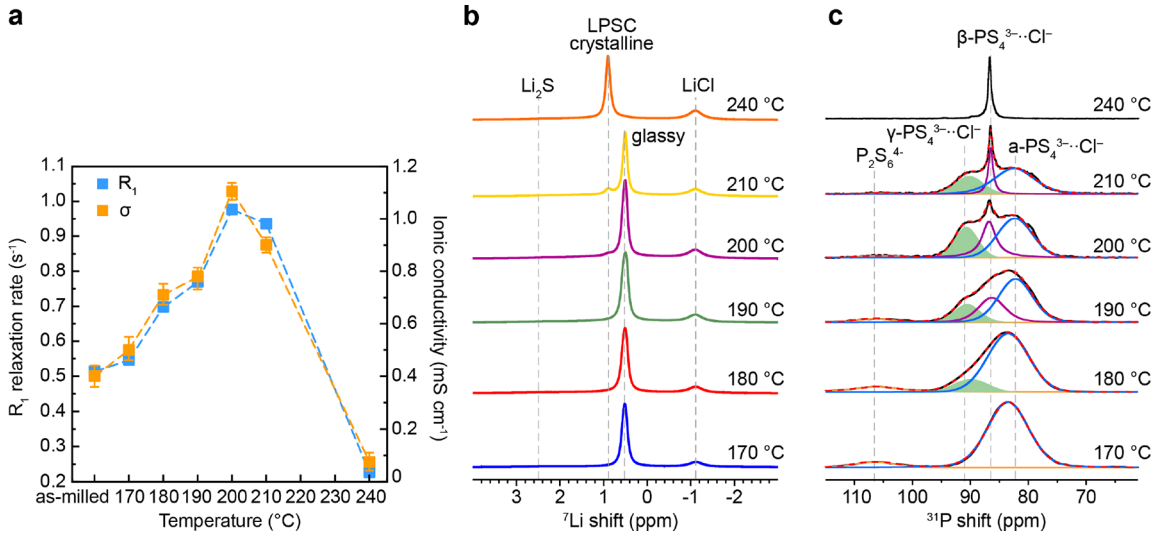

Figure 4. (a) Li-ion dynamics, ionic conductivities, and short-range structural order probed by ex-situ (b) ^{7}Li and (c) ^{31}P NMR of LPSCls (Li_3PS_4:LiCl = 2:1) synthesized at different temperatures (170, 180, 190, 200, 210, and 240 °C). The results suggest irreversible crystallization of the β-PS_4^{3-}···Cl^- phase when heated beyond 190 °C. The generation of the γ-PS_4^{3-}···Cl^- phase is correlated with increased ionic conductivity.

diffusion with ionic jump rates which are high enough to result in complete motional averaging. Overall, introducing Cl leads to different Li structural and dynamical attributes, while the long-range structural motifs of β-Li_3PS_4 and γ-Li_3PS_4 are partially adopted (Figure 1). The observation that ^{7}Li NMR resonance (0.5 ppm) of LPSCls lies in the middle of those from LPS (2 ppm) and LiCl (−1 ppm) suggests that Li^+ ions hop among PS_4^{3-} and Cl^- within the host lattice with a nearly equal residential time on each. Upon annealing at 240 °C, the LPSCl resonance shifts toward LPS, indicating a slightly higher affinity of Li^+ ion toward PS_4^{3-} ion, which can also be described as trapping.

^{31}P NMR spectra have been acquired for probing the anion sublattice. As shown in Figure 3b, the spectrum of the as-milled compound consists of two resonances: a resonance that resides at 83.5 ppm, attributed to PS_4^{3-} in amorphous Li_3PS_4, and a low-intensity resonance of $P_2S_6^{4-}$ at 106.4 ppm.[19,22,23] The 240 °C sample exhibits a sharp single resonance at 86.6 ppm, close to the resonance of β-Li_3PS_4 in LPS (Figure 3b, top). The narrower line shape of LPSCl (240 °C) suggests a more-ordered anion framework. The ^{31}P NMR spectrum of LPSCl (190 °C), shown in the middle of Figure 3b, exhibits diverse ^{31}P local environments. The three resonances are assigned to Cl-modified γ-PS_4^{3-} (90.8 ppm), β-PS_4^{3-} (86.7 ppm), and amorphous-PS_4^{3-} (82.2 ppm). It is worth mentioning that the Cl-modified γ-PS_4^{3-} has a ^{31}P NMR shift similar to $P_2S_7^{4-}$,[24] and we have confirmed the absence of $P_2S_7^{4-}$ in LPSCl from the Raman (Figure S2) and nPDF (Figure 2) results.

To probe the local environments around Cl in LPSCls, ^{35}Cl NMR is employed. The ^{35}Cl NMR spectra (Figure 3c) reveal that the Cl in LPSCls differs from LiCl(s), showing different ^{35}Cl shifts. Annealing LPSCl at a higher temperature drives Cl further away from the local environment of LiCl(s). At 240 °C, almost all the Cl resides in a crystalline framework, with a ^{35}Cl resonance at 9 ppm, similar to the shift of PS_3Cl^{2-} in our previous study on Cl-doped $Li_{2.5}Zn_{0.25}PS_4$.[25]

The rapid change in P environments (Figure 3b) suggests that fine-tuning the temperature is necessary for achieving an optimal anion substructure of LPSCls. Therefore, an additional four LPSCls (170, 180, 200, and 210 °C) are synthesized (Figure 4). As shown in Figure 3a, the Li in LPSCl (240 °C) is influenced by the surrounding crystalline lattice, showing a distinctive ^{7}Li shift vs the as-milled LPSCl. Figure 4b reveals that the crystalline phase occurs at 200 °C and gradually grows until 240 °C. This process is monitored with variable-temperature NMR (Figure S4). Li transition from the glassy to crystalline LPSCl with increasing temperature (172 °C to

https://doi.org/10.1021/acsmaterialslett.4c00488
ACS Materials Lett. 2024, 6, 2059−2064

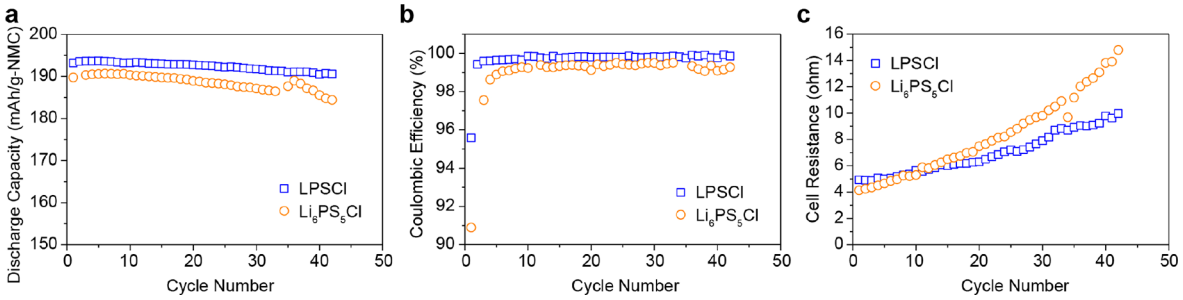

Figure 5. Applications of LPSCl (Li_3PS_4:LiCl = 2:1, 200 °C) and Li-argyrodite Li_6PS_5Cl as part of the catholytes in NMC622 | $Li_7P_2S_8I$ | Li ASSBs cycled with a current of 18.1 mA/g. (a) Discharge capacity, (b) Coulombic efficiency, and (c) cell resistance versus cycle number are presented with blue squares and orange circles for LPSCl and Li_6PS_5Cl argyrodite, respectively.

255 °C) is seen. However, the crystalline LPSCl is partially converted back to the glassy LPSCl after slow cooling during NMR data acquisition.

^{31}P NMR reveals that the anion frameworks start to alter at 180 °C with the occurrence of Cl-modified γ-PS_4^{3-} (Figure 4c). The rapid formation of Cl-modified β-PS_4^{3-} at 190 °C indicates that the anion substructures of LPSCl undergo a significant transition to a more disordered one (Figure 4c). With an elevated temperature, the fraction of Cl-modified β-PS_4^{3-} rises (Figure 4c) and reaches a maximum at 190 °C, then gradually decreases. Meanwhile, the line width of Cl-modified β-PS_4^{3-} becomes narrower, implying a higher crystallinity. At 240 °C, the nominal crystallinity is the highest (Figure S3). To explore the effects of Cl content on the sublattice structures, the ^{31}P and ^{7}Li NMR spectra of the samples with different LPS/LiCl ratios are compared (Figure S6). The ^{31}P spectra of LPS/LiCl = 1 and 3 remain a feature similar to LPS/LiCl = 2, suggesting no change in the anion frameworks. Meanwhile, the Li sublattice is maintained, revealed by the similar shape of ^{7}Li resonances.

Li^+-ion conductivities of different LPSCl samples are calculated using the Nyquist plot measured with EIS (Figure 4). Upon annealing, the measured conductivity increases and reaches a maximum of ∼1.1 mS/cm at 200 °C (Figure 4), more than double the as-milled LPSCl. Then, the ionic conductivity decreases with increasing temperature due to the crystallization (Figure S3).

To investigate the Li^+-ion mobility, ^{7}Li spin−lattice relaxometry is employed. The ^{7}Li R_1 (inverse of spin−lattice relaxation time constant, T_1) is calculated and presented, side by side, with the ionic conductivities in Figure 4a. According to a previous study of β-Li_3PS_4, at room temperature, the Li motional rate resides at the slow-motion regime,[22] where a shorter T_1 (larger R_1) corresponds to a faster motion. As shown in Figure 4a, the general trend of R_1 echoes that of conductivity, indicating that the conductivity is positively correlated to Li^+ ion motion in LPSCls. NMR T_1 relaxation times reflect ion dynamics on the time scale of 10^{-8} s, which corresponds to the high-frequency process, ∼MHz, of Li^+-ion transport in the bulk measured by EIS.[26] The similar trend of ion dynamics measured by NMR and ion transport determined by EIS suggests enhanced ion dynamics is the major contributing factor to the increased overall ionic conductivity. This trend is also shown in the different LPS/LiCl ratios (Figure S7), where the higher conductivity of LPS/LiCl = 3 arises from its highest Li^+ ion mobility.

The performance of LPSCl (Li_3PS_4:LiCl = 2:1, 200 °C) as a catholyte is evaluated in NMC622 | Li ASSBs (Figure 5). As shown in Figure 5a, the cell using LPSCl has a higher initial specific capacity than the argyrodite one (193.2 vs 189.7 mAh/g). After 42 cycles, the cells using LPSCl and argyrodite show a capacity retention of 98.7% and 97.2%, respectively. The LPSCl cell has an initial Coulombic efficiency (CE) of 95.6%, which is higher than that of the argyrodite cell (90.9%). At cycle 42, the CE of LPSCl cell is 99.9%, compared with 99.3% for the argyrodite one (Figure 5b). Therefore, LPSCl performs better than Li_6PS_5Cl argyrodite in ASSBs. Figure 5c shows that, after 42 cycles, the cell resistance of the LPSCl cell is increased by 103%, which is lower than 258% for the cell using argyrodite. The slower increase in cell resistance indicates that LPSCl is more stable against NMC622 than the argyrodite, which results in better cell performance.

In summary, novel Li_3PS_4-LiCl (LPSCls) glass-ceramic electrolytes are synthesized from inexpensive precursors. Neutron diffraction and MAS NMR reveal that LPSCls have unique structures: they partially adopt the long-range structures of β/γ-Li_3PS_4 while forming short-range structures distinctive from β/γ-Li_3PS_4. ^{31}P NMR results show a variety of Cl-modified PS_4^{3-} units in LPSCls: γ-PS_4^{3-}··Cl^-, β-PS_4^{3-}··Cl^-, and amorphous-PS_4^{3-}··Cl^-. All three types are observed in an intermediate temperature range [190 °C, 210 °C], where the anion sublattice is the most disordered and the ionic conductivity is the highest. The ^{7}Li spin−lattice relaxometry results reveal that the high conductivity is correlated with fast Li^+ ion motion. Li^+ ion shuffles among $PS_4^{3-}$and Cl^- anions with a similar affinity and diffuses rapidly through the diverse anion sublattice with a little barrier.

SYNTHESIS

LPSCl electrolytes were synthesized via planetary ball milling. Stoichiometric amounts of Li_2S (Sigma−Aldrich), P_2S_5 (Acros Organics), and LiCl (Sigma−Aldrich) were loaded into ZrO_2 milling jars with 5 mm ZrO_2 media and anhydrous xylene (Sigma−Aldrich) as a processing aid. Milling was carried out using a Retsch PM100 mill for 12 h at 500 rpm. After milling, xylene was removed under a vacuum at 70 °C for 2 h. The dry powder was then subjected to heat treatments in an argon environment, as described herein, and removed from the heating source immediately without controlled cooling.

NEUTRON DIFFRACTION

Room-temperature neutron total scattering experiments on the as-milled, 190 and 240 °C pre-annealed LPSC (Li_3PS_4:LiCl = 2:1) samples were performed at the Spallation Neutron Source at Oak Ridge National Laboratory (ORNL) at the NOMAD beamline (BL-1B). Approximately 0.5 g of powder for each

https://doi.org/10.1021/acsmaterialslett.4c00488
ACS Materials Lett. 2024, 6, 2059−2064

compound was sealed inside vanadium containers in a glovebox filled with dry argon. The acquisition time was 6 h for each sample. Then, background subtraction, flux normalization, and Placzek corrections were applied on the acquired data to generate the total scattering structural factor $S(Q)$. Using the IDL codes,[27] the $S(Q)$ was Fourier-transformed to the $G(r)$ within a Q range of 0.3−20 Å^{-1}. Neutron PDF simulation was obtained from PDFgui software. The structures of LiCl, β-Li_3PS_4, and γ-Li_3PS_4 were obtained from the ICSD database. U_{iso} was set to 0.05 for each atom. The calculation was performed at a Q_{max} value of 24 Å^{-1} at an r range of 0 to 10 Å^{-1}.

MAGIC-ANGLE-SPINNING NMR

^{7}Li and ^{31}P NMR magic-angle-spinning (MAS) NMR experiments were carried out with a Bruker Avance III-500 spectrometer. A three-channel 2.5-mm Bruker probe was tuned to 194.3 and 202.4 MHz for the measurements of ^{7}Li and ^{31}P, respectively. 2.5-mm rotors with powdered electrolyte samples packed inside were spun at 25 kHz. $\pi/2$-pulse was used to acquire the ^{7}Li spectra. The ^{7}Li shifts were referenced to LiCl(s) at −1.1 ppm. For ^{31}P NMR, a rotor-synchronized spin−echo sequence ($\pi/2-\pi$) was used, and the ^{31}P shifts were referenced to 85% H_3PO_4 solution at 0 ppm. ^{7}Li spin−lattice relaxation times were acquired based on the spectra collected using an inversion recovery pulse ($\pi-\tau-\pi/2$). ^{35}Cl NMR was performed on a 19.6-T magnet with a 3.2-mm home-built probe. The MAS rate was 16 kHz. The spectra were acquired using a spin−echo sequence. The shifts were referenced to LiCl(s) at 9.9 ppm. The variable-temperature MAS NMR was performed on a Bruker Avance III-500 spectrometer with a Bruker LAS MAS probe. The MAS rate was 5 kHz.

RAMAN SPECTROSCOPY

Raman spectra were collected on a Jasco Model NRS-3100 system, using a 532-nm laser at 6 mW of power. Data were collected in the range 150−700 cm^{-1} through a 5× microscope objective and 10 scans of 10 s each were accumulated. Raman shift was corrected with a silicon standard, and accuracy was estimated at ±2.5 cm^{-1}.

LABORATORY X-RAY DIFFRACTION

XRD patterns were collected in the range of 5°−40° 2θ, using a Bruker D8 Advance equipped with a Cu radiation source and LYNXEYE detector. Samples were prepared in custom air-free holders utilizing beryllium windows to eliminate air exposure. The step size was 0.02°/step, and the counting was 1 s/step.

DIFFERENTIAL SCANNING CALORIMETRY

Differential scanning calorimetry (DSC) measurements were performed using a microcalorimeter (TA Instruments, Model Discovery DSC-250). Approximately 5 mg of powder was sealed in an aluminum pan in an argon glovebox. Samples were scanned at 10 °C/min up to 400 °C.

IONIC CONDUCTIVITY MEASUREMENTS

Ionic conductivity was measured via impedance spectroscopy using a Biologic SP300 potentiostat/FRA. Approximately 350 mg of powder was pelletized under 300 MPa of pressure in custom pellet pressing hardware. A stack pressure of 8 MPa was applied during subsequent impedance measurements. Impedance spectra were collected from 7 MHz to 1 Hz with an AC amplitude of 100 mV. Ionic conductivity is determined from the measured real resistance of the pellet and the pellet dimensions.

ALL-SOLID-STATE BATTERY

The ASSBs were built using a Swagelok setup inside an argon-filled glovebox. The composite cathodes were prepared by mixing NMC622, LPSCl (Li_3PS_4:LiCl = 2:1, 200 °C)/Li_6PS_5Cl, and VGCF (67:30.5:2.5, wt %) in a mortar with pestle. First, the separator was made by compressing the $Li_7P_2S_8I$ solid electrolyte powder. Then, ∼0.05 g composite cathodes were applied and compressed onto the separator. Li metal chips were used as the anodes. A stacking pressure of ∼10 MPa and a current of 18.1 mAh/$g_{(NMC)}$ (0.09 C) were applied on the cells for the cycle life test with a voltage cutoff of [2.5 V, 4.3 V].

ASSOCIATED CONTENT

Supporting Information

The Supporting Information is available free of charge at https://pubs.acs.org/doi/10.1021/acsmaterialslett.4c00488.

Selected MAS NMR data, DSC data, EIS data, neutron PDF data, and Raman spectrum (PDF)

AUTHOR INFORMATION

Corresponding Authors

Yan-Yan Hu − *Department of Chemistry and Biochemistry, Florida State University, Tallahassee, Florida 32306, United States; Center of Interdisciplinary Magnetic Resonance, National High Magnetic Field Laboratory, Tallahassee, Florida 32310, United States;* orcid.org/0000-0003-0677-5897; Email: yhu@fsu.edu

Brian E. Francisco − *Solid Power, Inc., Louisville, Colorado 80027, United States*; Email: brian.francisco@solidpowerbattery.com

Authors

Pengbo Wang − *Department of Chemistry and Biochemistry, Florida State University, Tallahassee, Florida 32306, United States;* orcid.org/0000-0002-5740-6912

Sawankumar Patel − *Department of Chemistry and Biochemistry, Florida State University, Tallahassee, Florida 32306, United States;* orcid.org/0000-0002-5293-9330

Jason E. Roberts − *Solid Power, Inc., Louisville, Colorado 80027, United States*

Complete contact information is available at: https://pubs.acs.org/10.1021/acsmaterialslett.4c00488

Author Contributions

CRediT: **Pengbo Wang** conceptualization, data curation, formal analysis, investigation, methodology, validation, writing-original draft, writing-review & editing; **Sawankumar V Patel** data curation, formal analysis, investigation, methodology, software; **Jason E Roberts** data curation; **Brian E Francisco** conceptualization, data curation, formal analysis, investigation, resources, supervision, validation; **Yan-Yan Hu** conceptualization, methodology, formal analysis, investigation, project administration, supervision, writing-review & editing.

Notes

The authors declare no competing financial interest.

https://doi.org/10.1021/acsmaterialslett.4c00488
ACS Materials Lett. 2024, 6, 2059−2064

■ ACKNOWLEDGMENTS

The authors acknowledge the support from the National Science Foundation under Grant No. DMR-1847038 and from the NSF MRSEC program (No. NSF DMR-1720139). A portion of this work was performed at the National High Magnetic Field Laboratory, which is supported by National Science Foundation Cooperative Agreement No. DMR-2128556 and the State of Florida. A portion of this research used resources at the Spallation Neutron Source, a DOE Office of Science User Facility operated by the Oak Ridge National Laboratory.

■ REFERENCES

(1) Janek, J.; Zeier, W. G. A Solid Future for Battery Development. *Nat. Energy* **2016**, *1*, 16141.
(2) Randau, S.; Weber, D. A.; Kötz, O.; Koerver, R.; Braun, P.; Weber, A.; Ivers-Tiffée, E.; Adermann, T.; Kulisch, J.; Zeier, W. G.; Richter, F. H.; Janek, J. Benchmarking the Performance of All-Solid-State Lithium Batteries. *Nat. Energy* **2020**, *5*, 259−270.
(3) Gambe, Y.; Sun, Y.; Honma, I. Development of Bipolar All-Solid-State Lithium Battery Based on Quasi-Solid-State Electrolyte Containing Tetraglyme-LiTFSA Equimolar Complex. *Sci. Rep.* **2015**, *5*, 8869.
(4) Dixit, M.; Parejiya, A.; Essehli, R.; Muralidharan, N.; Haq, S. U.; Amin, R.; Belharouak, I. SolidPAC Is an Interactive Battery-on-Demand Energy Density Estimator for Solid-State Batteries. *Cell Rep. Phys. Sci.* **2022**, *3*, No. 100756.
(5) Liu, Y.; Meng, X.; Wang, Z.; Qiu, J. A Li $_2$ S-Based All-Solid-State Battery with High Energy and Superior Safety. *Sci. Adv.* **2022**, *8*, eabl8390.
(6) Wang, P.; Liu, H.; Patel, S.; Feng, X.; Chien, P.-H.; Wang, Y.; Hu, Y.-Y. Fast Ion Conduction and Its Origin in $Li_{6-x}PS_{5-x}Br_{1+x}$. *Chem. Mater.* **2020**, *32*, 3833−3840.
(7) Feng, X.; Chien, P.-H.; Wang, Y.; Patel, S.; Wang, P.; Liu, H.; Immediato-Scuotto, M.; Hu, Y.-Y. Enhanced Ion Conduction by Enforcing Structural Disorder in Li-Deficient Argyrodites $Li_{6-x}PS_{5-x}Cl_{1+x}$. *Energy Storage Mater.* **2020**, *30*, 67−73.
(8) Patel, S. V.; Banerjee, S.; Liu, H.; Wang, P.; Chien, P.-H.; Feng, X.; Liu, J.; Ong, S. P.; Hu, Y.-Y. Tunable Lithium-Ion Transport in Mixed-Halide Argyrodites $Li_{6-x}PS_{5-x}ClBr_x$: An Unusual Compositional Space. *Chem. Mater.* **2021**, *33*, 1435−1443.
(9) Wang, P.; Patel, S.; Liu, H.; Chien, P.; Feng, X.; Gao, L.; Chen, B.; Liu, J.; Hu, Y. Configurational and Dynamical Heterogeneity in Superionic $Li_{5.3}PS_{4.3}Cl_{1.7-x}Br_x$. *Adv. Funct. Mater.* **2023**, *33*, 2307954.
(10) Feng, X.; Chien, P.-H.; Patel, S.; Zheng, J.; Immediato-Scuotto, M.; Xin, Y.; Hung, I.; Gan, Z.; Hu, Y.-Y. Synthesis and Characterizations of Highly Conductive and Stable Electrolyte $Li_{10}P_3S_{12}I$. *Energy Storage Mater.* **2019**, *22*, 397−401.
(11) Rangasamy, E.; Liu, Z.; Gobet, M.; Pilar, K.; Sahu, G.; Zhou, W.; Wu, H.; Greenbaum, S.; Liang, C. An Iodide-Based $Li_7P_2S_8I$ Superionic Conductor. *J. Am. Chem. Soc.* **2015**, *137*, 1384−1387.
(12) Bui, A. D.; Choi, S.-H.; Choi, H.; Lee, Y.-J.; Doh, C.-H.; Park, J.-W.; Kim, B. G.; Lee, W.-J.; Lee, S.-M.; Ha, Y.-C. Origin of the Outstanding Performance of Dual Halide Doped $Li_7P_2S_8X$ (X = I, Br) Solid Electrolytes for All-Solid-State Lithium Batteries. *ACS Appl. Energy Mater.* **2021**, *4*, 1−8.
(13) Liu, Z.; Zinkevich, T.; Indris, S.; He, X.; Liu, J.; Xu, W.; Bai, J.; Xiong, S.; Mo, Y.; Chen, H. $Li_{15}P_4S_{16}Cl_3$, a Lithium Chlorothiophosphate as a Solid-State Ionic Conductor. *Inorg. Chem.* **2020**, *59*, 226−234.
(14) Poudel, T. P.; Deck, M. J.; Wang, P.; Hu, Y. Transforming Li_3PS_4 Via Halide Incorporation: A Path to Improved Ionic Conductivity and Stability in All-Solid-State Batteries. *Adv. Funct. Mater.* **2024**, *34*, 2309656.
(15) Han, F.; Yue, J.; Zhu, X.; Wang, C. Suppressing Li Dendrite Formation in $Li_2S−P_2S_5$ Solid Electrolyte by LiI Incorporation. *Adv. Energy Mater.* **2018**, *8*, 1703644.
(16) Iikubo, S.; Shimoyama, K.; Kawano, S.; Fujii, M.; Yamamoto, K.; Matsushita, M.; Shinmei, T.; Higo, Y.; Ohtani, H. Novel Stable Structure of Li_3PS_4 Predicted by Evolutionary Algorithm under High-Pressure. *AIP Advances* **2018**, *8*, 015008.
(17) Kaup, K.; Zhou, L.; Huq, A.; Nazar, L. F. Impact of the Li Substructure on the Diffusion Pathways in Alpha and Beta Li_3PS_4: An *in Situ* High Temperature Neutron Diffraction Study. *J. Mater. Chem. A* **2020**, *8*, 12446−12456.
(18) Liu, Z.; Fu, W.; Payzant, E. A.; Yu, X.; Wu, Z.; Dudney, N. J.; Kiggans, J.; Hong, K.; Rondinone, A. J.; Liang, C. Anomalous High Ionic Conductivity of Nanoporous β-Li_3PS_4. *J. Am. Chem. Soc.* **2013**, *135*, 975−978.
(19) Marchini, F.; Porcheron, B.; Rousse, G.; Albero Blanquer, L.; Droguet, L.; Foix, D.; Koç, T.; Deschamps, M.; Tarascon, J. M. The Hidden Side of Nanoporous β-Li_3PS_4 Solid Electrolyte. *Adv. Energy Mater.* **2021**, *11*, 2101111.
(20) Shiotani, S.; Ohara, K.; Tsukasaki, H.; Mori, S.; Kanno, R. Pair Distribution Function Analysis of Sulfide Glassy Electrolytes for All-Solid-State Batteries: Understanding the Improvement of Ionic Conductivity under Annealing Condition. *Sci. Rep.* **2017**, *7*, 6972.
(21) Smith, J. G.; Siegel, D. J. Low-Temperature Paddlewheel Effect in Glassy Solid Electrolytes. *Nat Commun* **2020**, *11*, 1483.
(22) Stöffler, H.; Zinkevich, T.; Yavuz, M.; Senyshyn, A.; Kulisch, J.; Hartmann, P.; Adermann, T.; Randau, S.; Richter, F. H.; Janek, J.; Indris, S.; Ehrenberg, H. Li^+-Ion Dynamics in β-Li_3PS_4 Observed by NMR: Local Hopping and Long-Range Transport. *J. Phys. Chem. C* **2018**, *122*, 15954−15965.
(23) Gobet, M.; Greenbaum, S.; Sahu, G.; Liang, C. Structural Evolution and Li Dynamics in Nanophase Li_3PS_4 by Solid-State and Pulsed-Field Gradient NMR. *Chem. Mater.* **2014**, *26*, 3558−3564.
(24) Seino, Y.; Nakagawa, M.; Senga, M.; Higuchi, H.; Takada, K.; Sasaki, T. Analysis of the Structure and Degree of Crystallisation of $70Li_2S−30P_2S_5$ Glass Ceramic. *J. Mater. Chem. A* **2015**, *3*, 2756−2761.
(25) Feng, X.; Chien, P.-H.; Patel, S.; Wang, Y.; Hu, Y.-Y. Enhanced Ion Conduction in $Li_{2.5}Zn_{0.25}PS_4$ via Anion Doping. *Chem. Mater.* **2020**, *32*, 3036−3042.
(26) Wilkening, M.; Heitjans, P. From Micro to Macro: Access to Long-Range Li^+ Diffusion Parameters in Solids via Microscopic ^{6,7}Li Spin-Alignment Echo NMR Spectroscopy. *ChemPhysChem* **2012**, *13*, 53−65.
(27) Neuefeind, J.; Feygenson, M.; Carruth, J.; Hoffmann, R.; Chipley, K. K. The Nanoscale Ordered MAterials Diffractometer NOMAD at the Spallation Neutron Source SNS. *Nucl. Instrum. Methods Phys. Res., Sect. B: Beam Interact. Mater. Atoms* **2012**, *287*, 68−75.

https://doi.org/10.1021/acsmaterialslett.4c00488
ACS Materials Lett. 2024, 6, 2059−2064